INTERNATIONAL JOURNAL OF APPLIED SCIENCE ENGINEERING AND MANAGEMENT

IJASEM

HIGH PERFORMANCE FREQUENCY CONVERTER CONTROLLED VARIABLE-SPEED WIND GENERATOR

[1]DR. A. GANGA DINESH KUMAR, [2] B. KEERTHANA, [3]K YAMINI, [4]B. SRAVANI

ABSTRACT

This work proposes a design scheme for arbitrary order discrete-time sliding mode observers for input-affine nonlinear systems. The dynamics of the estimation errors are represented in a pseudolinear form, where the coefficients of the characteristic polynomial comprise the nonlinearities of the algorithm. The design process is reduced to a state-dependent eigenvalue placement procedure. Moreover, two different discrete-time eigenvalue mappings are proposed. As basis for the eigenvalue mappings serves a modified version of the continuous-time uniform robust exact differentiator. Due on the chosen eigenvalue mapping the proposed algorithm does not suffer from discretization chattering. Global asymptotic stability of the estimation errors for observers of order 2 and 3 is proven and the method to prove stability for higher order observers is demonstrated. The performance of a 3-rd order observer is illustrated in simulation. Simulation studies indicate that proposed discrete-time observer might possess an upper bound of its convergence time independent of the initial conditionsThis article proposes an optimal control strategy with a view to achieving the best performance of a wind energy conversion system (WECS). The optimal control strategy depends on the linear-quadratic regulator (LQR) algorithm, which provides fast convergence and less mathematical intricacy The machine- and the grid-side converter/inverter are adjusted using the LQR controller. In this study, the system model and its control strategies are illustrated. Practical wind speed data are considered in this study for achieving realistic responses. The system performance is evaluated by comparing the results obtained using the LQR controller with that realized when the grey wolf optimizer algorithm-based optimized proportional-integral controllers are used, taken into account severe network disturbances. The simulation studies are extensively performed through the MATLAB/Simulinkjh environment that prove the validity of the LQR controller for improving the performance of the WECS. The simulation results are compared with the experimental results for more validation.

[1]PROFESSOR, [2,3&4] UG SCHOLAR
DEPARTMENT OF EEE,
MALLA REDDY ENGINEERING COLLEGE FOR WOMEN, HYDERABAD

I. OVERVIEW

When it comes to producing electricity, WIND power is often regarded as the primary clean energy option. The key causes that enable wind power to permeate

expected to reach a global total capacity of 840 GW by 2022 [1].

Wind power applications rely heavily on WTGSs with variable speeds because they are more reliable, produce less noise, and are more efficient than their fixed-speed counterparts. [2], [3].

The variable-speed WTGSs use a wide variety of electric machine types. Because of its self-excitation and high efficiency, the permanent-magnet synchronous generator (PMSG) has garnered a lot of attention in the contemporary wind business.

Full capacity frequency converters are used to connect the VS-WTGS that powers PMSG to the grid. Two power converters are used to create the frequency converter, and they are connected using a dc-link [3, 6]. Each of the six converters uses insulated gate bipolar transistors. A more costly and less dependable system, this architecture employs more regulated switches. To keep up with industrial demands, little effort has been put into researching and developing high-performance, simple, and dependable power converters with fewer power switches, lower losses, and lower costs.

In place of the conventional six-switch three-phase (SSTP) converter, a newer design called the four-switch three-phase (FSTP) converter is available. One advantage of the FSTP converter over the

the power networks are political problems, the depletion in fossil-fuel, and the growth in fuel costs. There was an 11% growth in total worldwide wind power capacity in 2017 to 539 GW [1]. Wind power is

SSTP converter is that it uses fewer switches (by a factor of three), has simpler driving circuits (since it has only two controlled branches and thus needs only two interface driving circuits), and has a lower maximum common mode voltage (by a factor of three) [7], [8].

Due to their reliability and large stability margins, proportional-integral (PI) controllers have long been used for controlling machine-side converters (MSCs) and grid-side inverters (GSIs) [3].

However, these controllers are very sensitive to the nonlinearity of the system and the uncertainty of the variables.

In [9–15], several methods are described for optimizing the PI controller designs. In order to improve the behavior of grid-tied WECSs, several algorithms have been proposed for designing proper values of multiple PI controllers under the cascaded structure. These algorithms include the shuffled frog leaping algorithm [10], the harmony search algorithm [11], the grey wolf optimization [3], the whale optimization algorithm [13], the gravitational search algorithm [14], and the water cycle algorithm [15].

When it comes to fine-tuning PI controllers, an evolutionary algorithm

known as the grey wolf optimizer (GWO) is where you want to be.

In the wild, grey wolves are represented by the GWO, a novel meta-heuristic optimization-based method [14].

The GWO algorithm is based on the hunting strategies of grey wolves, which are broken down into three stages—search, surround, and assault [16, 18]. Compared to other optimization methods, the GWO is distinguished by its straightforward implementation, free-derivative methodology, and less need for operator tweaks.

An alternative controller, the Linear-Quadratic Regulator (LQR), is introduced to obtain the highest dynamic performance and strong control stability while avoiding the complexities of traditional control techniques. LQR, in its most basic form, is a state-feedback controller that makes use of a state-space strategy for developing and regulating the system in question. Optimization in LQR controller is based on quadratic cost function minimization [19]. LQR controller's primary benefits are better performance with less complex algorithms and more computational analysis. The LQR controller is basic, straightforward, and requires less memory [20]. All of these positive aspects of the LQR are what led the researchers to choose it over more conventional controllers for their experiment. Many different types of industrial applications, including those in aerospace engineering and technology [21], discrete-time control systems [22], hybrid systems [23], laser beam shaping [24], electric motors [25], and wind energy systems [26], [27], have successfully implemented the LQR controller.

In order to enhance the qualities of a variable-speed WTGS linked to the grid, this research presents an optimum control strategy based on the LQR controller. In this article, we provide a cheap frequency converter built using two identical FSTP converters. A hysteresis current controller is evaluated for its potential to regulate the MSC and the GSI. For further cost and complexity reduction, a sliding mode observer (SMO) based rotor position estimator is constructed. The LQR controller's innovative application to the regulation of the FSTP converters of the VS-WTGS is the primary new contribution of this work. Both simulated and experimental data from grid disturbance circumstances are used to validate the proposed controller. Control strategies and the modeled system are shown. In this investigation, we take into account accurate wind speed data in order to generate believable results. Taking into consideration severe network fault situations, the performance of the system is measured by contrasting the results achieved using the proposed LQR controller with those realized while utilizing the GWO algorithm-based optimized PI controllers. MATLAB/Simulink is used to do the simulations that prove the LQR controller works as intended.

II. WIND TURBINE MODEL

The mathematical expression for the amount of power drawn from the wind is [28] [30].

$$P_\omega = 0.5\rho\pi R^2 V_\omega^3 C_P(\lambda, \beta) \tag{1}$$

where P is the wind power output (in watts), the air density (in kilograms per

cubic meter), R the blade radius (in meters), V the wind speed (in meters per second), C the power coefficient (in degrees per second), and the tip speed ratio (in degrees).
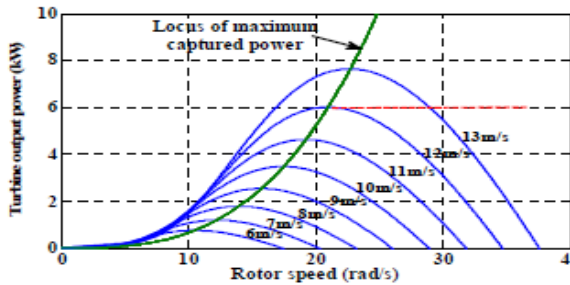

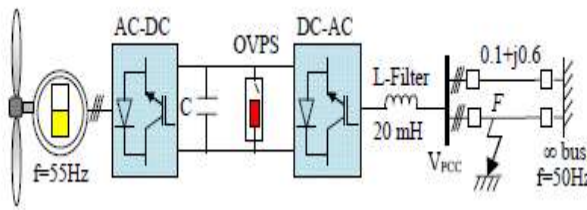*Fig. 1. Wind turbine characteristics with MPPT.*

Fig. 2. Model system.

The C coefficient can be described as follows [3]:

$$C_P(\lambda, \beta) = 0.5(\lambda - 0.022\beta^2 - 5.6)e^{-0.17\lambda} \qquad (2)$$

where is the rotor blade speed in revolutions per second.

Maximum power point tracking (MPPT) in a wind turbine is seen in Fig. 1. The following [6] describes the rotor speed at which the highest amount of power is extracted from the wind:

$$P_{max} = 0.5\rho\pi R^2 \left(\frac{\omega_T R}{\lambda_{opt}}\right)^3 C_{P-opt} \qquad ($$

in which the best possible values for C and are indicated by C and.

MODEL SYSTEM III

The effectiveness of the suggested LQR controller used to fine-tune the frequency

converter of the VSWT driving PMSG is shown using a system model, as shown in Fig. 2. A VSWT, a PMSG with a full-capacity frequency converter, and a double-circuit transmission line make up the VSWT-PMSG system. In this analysis, the PMSG is designed to operate at 6.0 kW and 55 Hz. Additional information on the PMSG data is provided in [28].

DISCRETE SMO

The implementation of the above mentioned differentiator can be seen as observer for an integrator chain. The observer proposed in this paper is a generalization of the discretized differentiator

Discrete-time eigenvalue mapping In the following subsections the proposed observers are designed such that the eigenvalues (14) of the pseudo-linear continuous-time system are mapped to discrete-time eigenvalues of the corresponding discrete-time system. The eigenvalue mappings used in this work ensure that there exists no discretization chattering in the unperturbed case. In Section 5 it will be shown that only the lower and upper bounds of the state-dependent discrete-time eigenvalues are crucial for the proof of global asymptotic stability of the origin of the observer errors. Hence, various discrete-time eigenvalues are possible. Taking the proposed continuous-time eigenvalues for

order n (14) into account, the semi-implicit eigenvalue mapping proposed in [39] yields the discrete-time eigenvalues

$$z_n = z_s(e_{n,k}) = \frac{|e_{n,k}|^{\frac{1}{n}}}{hp_1\mu|e_{n,k}| + |e_{n,k}|^{\frac{1}{n}} + hp_1},$$

while the matching eigenvalue mapping proposed in [37] yields

$$z_n = z_m(e_{n,k}) = \exp\left(-hp_1\frac{1 + \mu|e_{n,k}|}{|e_{n,k}|^{\frac{1}{n}}}\right)$$

where h is the constant sampling time and $e_{n,k}$ is the difference between the measured and the estimated signal and is defined in the following subsection. In Fig. 1 the two different eigenvalue mappings as function of $e_{n,k}$ for n = 2 are illustrated. The parameters are chosen as h = 1, μ = 1 and p_1 is chosen separately
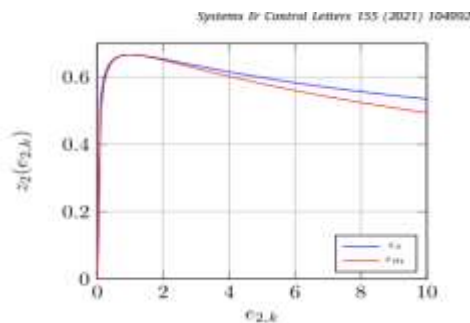

Fig: Discrete-time eigenvalue mappings (15) and (16) as function of the observer output error $e_{2,k}$.
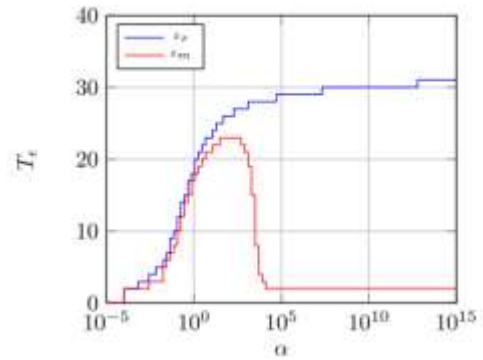

Fig: Practical convergence time as function of the initial observer errors for the eigenvalue mappings (15) and (16).

Strategy for modeling and controlling frequency converters

The electrical setup of the proposed VSWT-PMSG topology is shown in Fig. 4 of this work. Fig. 4 depicts the VSWT-PMSG frequency converter, which comprises of a two-split capacitor in the dc-link and two identical FSTP power converters (one for the converter and one for the inverter). A
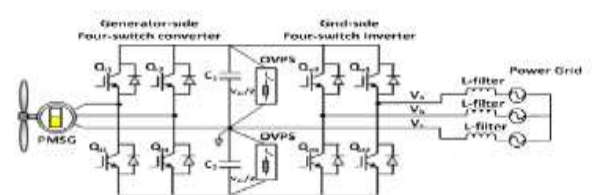

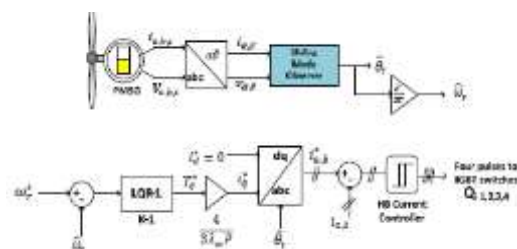
Fig. 4. Electrical configuration of VSWT-PMSG.

Fig. 5. Control blocks for the MSC.

The two-split capacitor in an FSTP inverter allows for voltage and frequency to be adjusted in a balanced, three-phase

output to the grid. The terminals of the generator are connected straight to the midpoint of the two-split capacitor and the two pulse width modulation voltages of the converter. The output of the two-leg inverter is connected to the three-phase electrical grid at the same midway.

The converter/inverter's third phase is represented by the split-capacitor's halfway.

This control technique is simple, but effective in terms of dynamic responsiveness [7]. Output phase voltages of the FSTP inverter are given in a matrix form as a function of the switching states, S and S of the power switches and the voltage across the two-split capacitor, V.

$$\begin{bmatrix} V_a \\ V_b \\ V_c \end{bmatrix} = \frac{V_{dc}}{3} \begin{bmatrix} 4 & -2 \\ -2 & 4 \\ -2 & -2 \end{bmatrix} \begin{bmatrix} S_a \\ S_b \end{bmatrix} + \frac{V_{dc}}{3} \begin{bmatrix} -1 \\ -1 \\ 2 \end{bmatrix} \quad (16)$$

1. The MSC

The MSC is in charge of transferring all of the electricity generated by the wind turbine to the power grid. In order to accomplish this goal, a hysteresis current controller is used, which makes the estimated generator speed () follow the reference speed (). The LQR controller uses the difference in the reference and measured speeds as input to produce the torque instruction (T. To regulate active power, the q-axis current (i) is determined by the temperature (T). To get maximal torque with least current, we set i to zero.

This means that the PMSG's resistive losses may be reduced.

Using the calculated rotor angle (), the dq-axes current quantities are transformed into the three-phase reference currents.
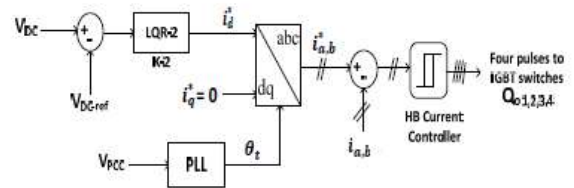
The PMSG's detected two-phase currents (i,) are

Fig. 6. Control blocks for the GSI.

two hysteresis comparators were used to evaluate the reference currents (i,) against the two-phase reference currents. These comparators' output signals trigger the four electrical switches. Fig. 5 shows a block schematic of the MSC.

The GSI, in B.

The primary function of the GSI is to execute a unity power factor operation at the grid by adjusting the dc-link voltage (V) and maintaining it at the correct value. In this analysis, we take into account two dc-link capacitors, each with a rated value of 500 F, and set the V to 700 V. The hysteresis current controller is used to run the GSI, and in this case the V is regulated such that it follows the dc-link reference voltage (V. The LQR controller generates the d-axis current (i) based on the error signal between the reference and real dc-link voltages. The reactive power may be modulated by the i. Therefore, it is zeroed out to ensure that the grid terminals are operating at a power factor of 1. The phase locked loop (PLL) system uses the voltages at the point of common coupling (V) to convert the currents along the dq - axes into the abc components, with the transformation angle). The firing pulses for the two-leg inverter are generated by two separate hysteresis comparators, which compare the grid-side actual two-

phase currents (i,) with the two-phase current instructions (i,). GSI control's block diagram is shown in Fig. 6 [32]-[34].

The Suggested Regulators

The LQR controller, A.

Using a state-space system form, the LQR is an optimum controller that may improve the system's response with the help of a carefully selected state-feedback gain matrix (K). To find out what K should be, we employ a pole positioning technique that takes the intended pole placement into account. The LQR is an excellent option for higher order and multi-input systems where the optimal response of the closed-loop system is attained, but the values of matrix (K are straightforward to compute using this approach.

The best pole placement for LQR is defined by the cost function. It reduces the cost function by solving a system of differential equations depicting the pathways of the control variables. Minimizing the quadratic cost function (J) is the goal, and the control input u) is what makes it a reality.

$$J = \int_0^\infty (x_e^T Q x_e + u_c^T R u_c)\, dt$$

where Q and R are the weighted-matrices that are chosen to produce poles in the desired position. When Q is big, the closed-loop poles (E, A, BK) shift to the left in the s-plane. This causes the error to quickly approach zero. When Q and R are both positive semi-definite matrices, then K is found by picking the right weighted-matrix.

To minimize the quadratic cost function J, the following control input is chosen:

$$u_c = -Kx_e \tag{18}$$

Where

$$x_e = x_{ref} - x_{actual}.$$

The design of the optimal control scheme is realized by solving
the Algebraic Riccati Equation:

$$A^T P + PA - PBR^{-1}B^T P + Q = 0 \tag{19}$$

Thus, the optimal K is obtained as:

$$K = R^{-1}B^T P \tag{20}$$

In this investigation, the control system is linearized in the
state-space form as follows:

$$\dot{X} = AX + BU \tag{21}$$

$$Y = CX \tag{22}$$

where X refers to the state variables, U represents the control
input, and Y represents the control output. For the PMSG model, the X, U, and Y can be expressed as
Follows:

$$X = \begin{bmatrix} i_{d-PMSG} & i_{q-PMSG} & \omega_e \end{bmatrix}^T \tag{23}$$

$$U = \begin{bmatrix} v_{ds-PMSG} & v_{qs-PMSG} & \lambda_m \end{bmatrix}^T \tag{24}$$

$$Y = \begin{bmatrix} i_{d-PMSG} & i_{q-PMSG} & \omega_e \end{bmatrix}^T \tag{25}$$

For the power grid model, the X , U , and Y are written as
Follows:

$$X = \begin{bmatrix} i_{d-Grid} & i_{q-Grid} \end{bmatrix}^T \tag{26}$$

$$U = \begin{bmatrix} v_{ds-Grid} & v_{qs-Grid} \end{bmatrix}^T \tag{27}$$

$$Y = \begin{bmatrix} i_{d-Grid} & i_{q-Grid} \end{bmatrix}^T \tag{28}$$

where v and v represent the network voltages along the dq axis.

The performance metric J in this study is the difference between the set-point and real signals. The LQR controller takes in the error signal as its input. For the LQR-1 shown in Fig. 5, the torque command (T) is the result of the LQR controller's processing of the reference signal () and the measured signal ().

In order to achieve maximum efficiency without breaking the bank, the following values were selected for Q and R:

Q = [Q-1 Q-2] = [1.18 10] ; R = [R-1 R-2] = [0.7 2].

To get the ideal gain K, the linearized system is used to calculate the values of A and B, which are then input into the MATLAB function [K] = LQR (A, B, Q, R). For the considered system, the values of K are calculated as follows:

K = [K-1 K-2] = [1.2984 2.2361].

GWO algorithm optimized PI controller B.

Grey wolf optimization (GWO) is a new population-based method introduced in 2014. The grey wolf formerly frequented pack territories. Typically, there are five to twelve wolves in a pack. The four most prominent varieties within this social group are designated by the Greek letters alpha (), beta (), delta (), and omega (). The alpha wolves symbolize the pack's leaders. They are in charge of managing daily tasks like going on a hunt, finding a good sleeping spot, and waking up at the right time. Also, in an apparent effort at democracy, the wolves will go for members of their own pack. The wolves are the next tier up in the pack, providing assistance and backing to the wolves as they make judgments. When wolf passes away or is too old to be effective, wolf is the most qualified to take over. The wolves are the ones who should aid the wolves and assist to maintain the pack's hierarchy. The alpha wolves are the top dogs in the pack; they get the last scraps of food.

Wolves are sometimes the group's designated babysitters. The wolves are in charge of educating the and wolves, but the wolves are under their thumb. The hunt of a grey wolf may be broken down into the following stages, as described by [16]–[18]:

1. locating, pursuing, and closing in on one's victim.

To capture an animal, one must first encircle it and then annoy it until it gives up and stops moving.

Third, make an assault on the victim.

In this research, the PI controller settings are designed using the GWO technique, as described in [3].

CONCLUSIONS AND IMPLICATIONS

The MATLAB/Simulink environment is used to conduct the simulation analyses. The time interval is assumed to be 20 s. Analysis is performed taking into account both steady-state and transient operating situations to compare the LQR controller's performance to that achieved by using the GWO-based optimum PI controllers.

A. Optimal Working Conditions

Using real-world wind speed data measured at Egypt's Zaafarana wind farm,

Fig. 7(a) demonstrates the dynamic reaction of the VSWT powered PMSG. With a simulation length of 500 s, this research takes into account wind speeds from 8.1 m/s to 11.8 m/s. Responses of the observed and anticipated generator speeds are shown in Fig. 7(b). It is important to note that the predicted PMSG speed might be closely matched by the observed speed. Responses of the PMSG's measured and predicted rotor locations are shown in Fig. 7(c). Notably, the SMO method can reliably predict the PMSG's rotor position/speed in any setting. Maximum and active grid power are shown in Fig. 7(d). Keep in mind that owing to the power losses of converters, those powers are quite near. Reactive power at the GSI under LQR control is shown in Fig. 7(e). At the PCC, the terminal grid voltage is shown in Fig. 7(f). For an example of the terminal grid current at the PCC, see Fig. 7(g). Particularly advantageous is the compatibility between the VSWT-PMSG system and the FSTP frequency converter. under addition, the LQR controller can reliably supply the highest possible amount of wind power to the utility grid under a variety of situations.
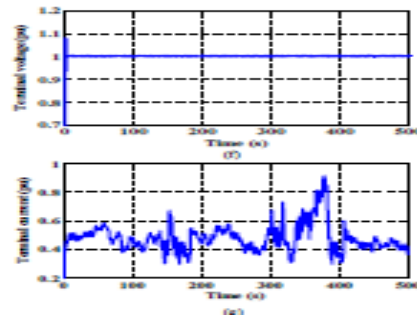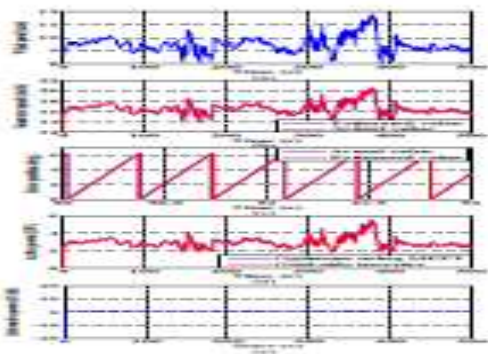

Fig. 7. Performances of LQR controllers with the help of using practical wind
speed data (a) Wind speed. (b) Generator speed. (c) Rotor position of the
PMSG. (d) Active power of the grid-side inverter. (e) Reactive power of the
grid-side inverter. (f) Terminal grid voltage. (g) Terminal grid current.

Operating Condition B: Transient Fault

Putting the system through rigorous grid disturbance tests the robustness of the LQR controller-adjusted power converters of the VSWT-PMSG that has been introduced into the network.

As can be seen in Fig. 1, the 3LG fault occurs at 1.5 s, specifically at the fault site F. This transmission line's circuit breakers (CBs) are opened simultaneously at 1.6 s to clear the problem. The problem is repaired after 1.7 s, and the CBs reclose in unison after 2.5 s. There has been no change in the wind speed from 12 m/s. An overvoltage protection mechanism (OVPS), as described in [28], is used in this study under fault conditions. Figure 8(a) illustrates the differences in Vdc responses between the two methods, with and without the use of OVPS. The rapid rise in Vdc at the time of the failure is shown. Therefore, the Vdc is presumed to be maintained within allowable limits by the OVPS. Figure 8(b) highlights the chopper current response. Figure 8(c) shows how the terminal grid voltage at the PCC responds with the LQR controller, which is superior than the optimized PI

controller based on the GWO method. Figure 8(d) depicts the reactive power responses of the GSI for both methods. When compared to the ideal PI control method, the LQR control technique results in a greater improvement in reactive power response at the GSI.

VIII. RESULTS OF EXPERIMENTS

The suggested method for enhancing LQR LVRT performance is verified using a compact experimental setup in the lab. In this configuration, two permanent-magnet synchronous motors are connected together. Both machines function as motors; the first simulates the action of a wind turbine, while the second generates electricity. Two-level IGBT regulates PMSM speed.
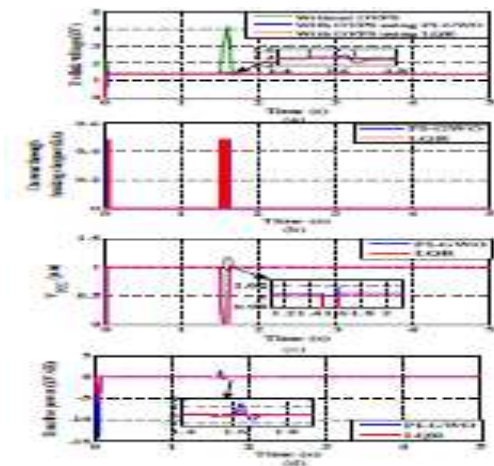

Fig. 8. Performances for 3LG fault (a) DC-link voltage. (b) Current through chopper. (c) Terminal grid voltage at the PCC. (d) Reactive power of the grid-side inverter.

powered by a 7 HP Danfoss FC 302 industrial motor. The power for the PMSM generator comes from its own autotransformer. The PMSG is managed in the same way, with the same drive, but with a different hardware configuration that provides access to the IGBT gates for use with external controllers. The GSC

gates are also controlled by a third drive. Cinergia GE-15 grid emulator [35] is used to get the GSC and MSC power supply and grid voltage fault circumstances. Drive brake feature is used to implement OVP by connecting a chopper circuit with a high power ratings resistor in parallel with the dc-link capacitor. The currents and voltages in the system are measured by the blocks of sensors responsible for taking these readings. A torque meter attached to the coupling point reads the PMSG torque, and a rotary incremental encoder attached to the PMSM shaft reads the angular position at a rate of 1024 pulses per revolution. A dspace 1202 MicrolabBox DSP board runs the control schemes. Parameters for the PMSG experimental setup are listed in Table I, which corresponds to the PMSG experimental configuration seen in Fig. 9(a). The experimental configuration includes the LQR controller. Table II displays a comparison between the benefits made by the system when controlled by the GWO-based PI controller and the LQR controller.

By lowering the nominal grid voltage for a set amount of time, the grid emulator may simulate the length of a problem. The Vdc response of the system is shown in Fig. 9(b) for a fault with a duration of 100 ms and a magnitude of 10%. What this number proves

TABLE I
PMSG EXPERIMENTAL SETUP PARAMETERS.

Parameters	Values
Nominal voltage	117 V rms (ph-to-n)
System frequency	50 Hz
Dc-link voltage	350 V
Dc-link capacitance	350 μF
Filter inductance	3.3 mH
Grid inductance	0.8 mH
PMSG rated power	5 kW
Number of poles	22
PMSG rated speed	240 rpm
PMSG winding resistance	0.84 Ω
PMSG winding d-axis inductance	12.6 mH
PMSG winding q-axis inductance	21.8 mH

TABLE II
CONTROLLER GAINS USING GWO

Controllers Gains	Notation	
Vdc outer-loop proportional gain	Kp_{Vdc}	
Vdc outer-loop integral gain	Ki_{Vdc}	
Vpcc outer-loop proportional gain	Kp_{Vpcc}	
Vpcc outer-loop integral gain	Ki_{Vpcc}	
Inner - loop proportional gain	Kp_{GSC}	
Inner - loop integral gain	Ki_{GSC}	

the failure response of the system's dc-link voltages. To demonstrate the dynamic reaction, a 324 V vertical offset has been introduced. Vdc*, the reference voltage for the dc connection, has been set at 350V. The accuracy of the voltage regulation with respect to the reference value is seen clearly in Fig. 9(b). At t=0.8 s, when the fault occurs, Vdc drops before rising again. The OVP has detected a drop in power at the fault location. However, the rise happens when the fault is fixed and Vdc is brought back up to its normal level under conscious control. The Vdc response reveals how the control strategy affects the system's performance. When compared to the GWO controller, the LQR controller has less of an effect on the Vdc drop, less overshoot, and quicker recovery after a malfunction.

The Vpcc reaction is seen in Fig. 9(c) during the fault. To illustrate the dynamic response of Vpcc, a vertical offset of 105 V has been applied. 117 rms is used as the rms voltage reference, or Vpcc*.

During a fault, the rms voltage will decrease. When a fault occurs, Vpcc resets to Vpcc*. The LQR controller's controller improvements similarly improve both transient and steady-state performances. Active power response during the fault is shown in Fig. 9(d). The voltage to active power ratio is 1 in the channel charts. Due to the short length of the fault, it is believed that the wind speed remains constant throughout.

For this reason, we'll be doing this test with the PMSG torque reference set to 100 N.m and the rotational speed held steady at 150 rpm. During a failure, the active power of the grid drops, but it quickly recovers to its pre-fault level. The reaction time of the LQR controller is much shorter and more uniform than that of the GWO. It is clear from the chopper resistor current that the OVP chopper resistor is only activated when a problem occurs.

During the fault, the reactive power response is seen in Fig. 9(e). The ratio of voltage to reactive power is 1 in the channel charts.

During a malfunction, the reactive power support is increased to aid in maintaining Vpcc. Figure 9(e) shows that the LQR controller has a greater impact on voltage responses because it supplies more grid reactive power than the GWO controller.
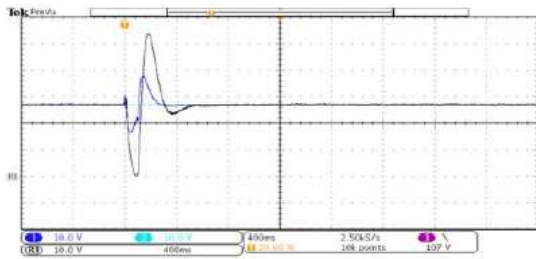
Fig. 9(b). Vdc response to fault (Ch-1 Vdc LQR, Ch-2 Vdc, R1 Vdc GWO).*
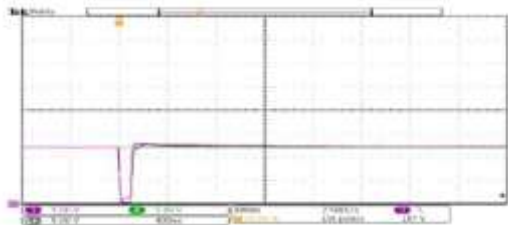

Fig. 9(c). Vpcc response to fault (Ch-3 Vpcc LQR, Ch-4 Vpcc, R2 Vpcc GWO).*
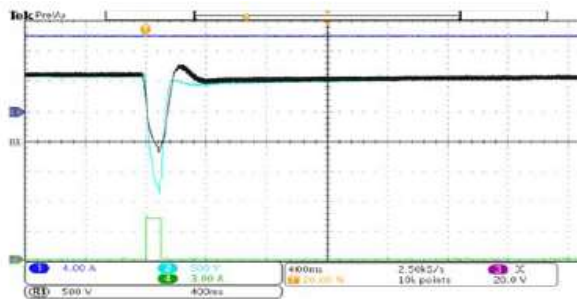

Fig. 9(d). Active power response to fault (Ch-1 IqPMSG, Ch-2 PGSC LQR, R1 PGSC GWO, Ch-4 Current through the chopper resistor).
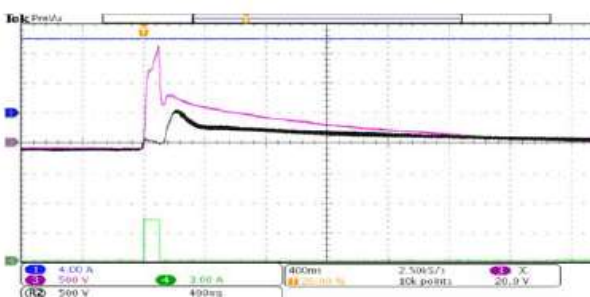

Fig. 9(e). Reactive power response to fault (Ch-1 IqPMSG, Ch-3 QGSC LQR, R2 QGSC GWO, Ch-4 Current through the chopper resistor).

IX. CONCLUSION

A new design scheme for arbitrary order sliding mode observer for nonlinear input-affine systems has been proposed, where the design procedure of the sliding mode algorithm is reduced to state-dependent eigenvalue placement. Two discretetime eigenvalue mappings have been proposed, which all suppresses discretization chattering. Simulation studies indicate that the proposed observer possesses an upper bound of its practical convergence time of its estimation errors. It is proven that for order 2 and 3 the estimation errors converge to the origin in the unperturbed case. Furthermore, the method to prove global asymptotic stability for higher order observers (n ≥ 4) has been demonstrated. The proposed observer for order n = 3 was evaluated in simulation studies and was compared to a classical Luenberger observer and a discrete-time High gain observer. Additionally, the performance of the observer was demonstrated on a 4th order system.

REFERENCES

[1] S.K. Spurgeon, Sliding mode observers: a survey, Internat. J. Systems Sci. 39 (8) (2008) 751–764, http://dx.doi.org/10.1080/00207720701847638.

[2] A. Levant, Higher-order sliding modes, differentiation and output-feedback control, Internat. J. Control 76 (9–10) (2003) 924–941, http://dx.doi.org/10.1080/0020717031000099029.

[3] V. Utkin, Variable structure systems with sliding modes, IEEE Trans. Autom. Control 22 (2) (1977) 212–222, http://dx.doi.org/10.1109/tac.1977.1101446.

[4] S. Spurgeon, R. Patton, Robust variable structure control of model reference systems, IEE Proc. D Control

Theory Appl. 137 (6) (1990) 341, http://dx.doi.org/10.1049/ip-d.1990.0045.

[5] J. Davila, L. Fridman, A. Levant, Second-order sliding-mode observer for mechanical systems, IEEE Trans. Autom. Control 50 (11) (2005) 1785–1789, http://dx.doi.org/10.1109/tac.2005.858636.

[6] E.A. Misawa, J.K. Hedrick, Nonlinear observers—a state-of-the-art survey, J. Dyn. Syst. Meas. Control 111 (3) (1989) 344–352, http://dx.doi.org/10.1115/1.3153059.

[7] J.A. Moreno, M. Osorio, A lyapunov approach to second-order sliding mode controllers and observers, in: 2008 47th IEEE Conference on Decision and Control, IEEE, 2008, http://dx.doi.org/10.1109/CDC.2008.4739356.

[8] C. Edwards, S.K. Spurgeon, On the development of discontinuous observers, Internat. J. Control 59 (5) (1994) 1211–1229, http://dx.doi.org/10.1080/00207179408923128.

[9] C. Edwards, S.K. Spurgeon, Robust output tracking using a sliding-mode controller/observer scheme, Internat. J. Control 64 (5) (1996) 967–983, http://dx.doi.org/10.1080/00207179608921668.

[10] C. Edwards, S.K. Spurgeon, R.J. Patton, Sliding mode observers for fault detection and isolation, Automatica 36 (4) (2000) 541–553, http://dx.doi.org/10.1016/s0005-1098(99)00177-6.

[11] C.P. Tan, C. Edwards, Sliding mode observers for detection and reconstruction of sensor faults, Automatica 38 (10) (2002) 1815–1821, http://dx.doi.org/10.1016/s0005-1098(02)00098-5.

[12] T. Floquet, C. Edwards, S. Spurgeon, On sliding mode observers for systems with unknown inputs, in: 2006 International Workshop on Variable Structure Systems (VSS), IEEE, 2006, http://dx.doi.org/10.1109/vss.2006.1644520.

[13] X.-G. Yan, C. Edwards, Nonlinear robust fault reconstruction and estimation using a sliding mode observer, Automatica 43 (9) (2007) 1605–1614, http://dx.doi.org/10.1016/j.automatica.2007.02.008.

[14] C.C. de Wit, J.-J. Slotine, Sliding observers for robot manipulators, Automatica 27 (5) (1991) 859–864, http://dx.doi.org/10.1016/0005-1098(91)90041- y.

[15] J. Hernandez, J.-P. Barbot, Sliding observer-based feedback control for flexible joints manipulator, Automatica 32 (9) (1996) 1243–1254, http://dx.doi.org/10.1016/0005-1098(96)00069-6